Spin-orbit entangled $j = \frac{1}{2}$ moments in Ba_2CeIrO_6: A frustrated fcc quantum magnet

A. Revelli,[1] C. C. Loo,[1] D. Kiese,[2] P. Becker,[3] T. Fröhlich,[1] T. Lorenz,[1] M. Moretti Sala,[4] G. Monaco,[5] F. L. Buessen,[2] J. Attig,[2] M. Hermanns,[6,7] S. V. Streltsov,[8,9] D. I. Khomskii,[1] J. van den Brink,[10] M. Braden,[1] P. H. M. van Loosdrecht,[1] S. Trebst,[2] A. Paramekanti,[11] and M. Grüninger[1]

[1]*Institute of Physics II, University of Cologne, 50937 Cologne, Germany*
[2]*Institute for Theoretical Physics, University of Cologne, 50937 Cologne, Germany*
[3]*Sect. Crystallography, Institute of Geology and Mineralogy, University of Cologne, 50674 Cologne, Germany*
[4]*Dipartimento di Fisica, Politecnico di Milano, I-20133 Milano, Italy*
[5]*Dipartimento di Fisica, Università di Trento, I-38123 Povo (TN), Italy*
[6]*Department of Physics, Stockholm University, AlbaNova University Center, SE-106 91 Stockholm, Sweden*
[7]*Nordita, KTH Royal Institute of Technology and Stockholm University, SE-106 91 Stockholm, Sweden*
[8]*M.N. Mikheev Institute of Metal Physics, Ural Branch, Russian Academy of Sciences, 620137 Ekaterinburg, Russia*
[9]*Ural Federal University, 620002 Ekaterinburg, Russia*
[10]*Institute for Theoretical Solid State Physics, IFW Dresden, 01069 Dresden, Germany*
[11]*Department of Physics, University of Toronto, Toronto, Ontario Canada M5S 1A7*

(Received 18 January 2019; revised manuscript received 21 July 2019; published 26 August 2019)

We establish the double perovskite Ba_2CeIrO_6 as a nearly ideal model system for $j = 1/2$ moments, with resonant inelastic x-ray scattering indicating that the ideal $j = 1/2$ state contributes by more than 99% to the ground-state wave function. The local $j = 1/2$ moments form an fcc lattice and are found to order antiferromagnetically at $T_N = 14$ K, more than an order of magnitude below the Curie-Weiss temperature. Model calculations show that the geometric frustration of the fcc Heisenberg antiferromagnet is further enhanced by a next-nearest neighbor exchange, and a significant size of the latter is indicated by *ab initio* theory. Our theoretical analysis shows that magnetic order is driven by a bond-directional Kitaev exchange and by local distortions via a strong magnetoelastic effect. Both, the suppression of frustration by Kitaev exchange and the strong magnetoelastic effect are typically not expected for $j = 1/2$ compounds making Ba_2CeIrO_6 a riveting example for the rich physics of spin-orbit entangled Mott insulators.

DOI: 10.1103/PhysRevB.100.085139

I. INTRODUCTION

Spin-orbit entangled Mott insulators stand out in the growing family of quantum materials with strong spin-orbit coupling for their correlation-driven phenomena [1]. Of particular interest are materials with partially filled $4d$ and $5d$ orbitals, such as the iridates, in which the formation of local $j = 1/2$ moments is an iridescent source of rich physics [2]. The spin-orbit entangled wave function of these Kramers doublets gives rise to fundamentally different types of exchange interactions depending on the geometric arrangement of the elementary octahedral IrO_6 building blocks [3–5]. Corner-sharing octahedra yield isotropic Heisenberg exchange, which has been explored as a potential source of spin-orbit assisted superconductivity [6–10] in the context of Sr_2IrO_4 [11,12], an isostructural analog of the high-T_c parent compound La_2CuO_4. Edge-sharing octahedra, in contrast, give rise to Kitaev-type bond-directional exchange, which has initiated an intense search for spin-orbit driven frustrated quantum magnetism in so-called Kitaev materials [13] such as the honeycomb iridates Na_2IrO_3, α-Li_2IrO_3, and $H_3LiIr_2O_6$ [14–16] and the related α-$RuCl_3$ [17]. Possibly the most spectacular experimental result in this realm is the recent claim of a quantized thermal Hall effect in α-$RuCl_3$ [18], a direct signature of the long sought-after Kitaev spin liquid [19].

In this paper, we first demonstrate experimentally that the double perovskite Ba_2CeIrO_6 is a nearly ideal realization of a $j = 1/2$ Mott insulator, forming a model system for frustrated quantum magnetism on the fcc lattice. Our x-ray diffraction results show a global cubic $Fm\bar{3}m$ structure, while resonant inelastic x-ray scattering (RIXS) reveals a small noncubic distortion resulting in a ground-state wave function which overlaps by more than 99% with the ideal cubic $j = 1/2$ state. The magnetic susceptibility shows an antiferromagnetic ordering temperature $T_N = 14$ K which is suppressed by more than an order of magnitude compared to the Curie-Weiss temperature $|\Theta_{CW}|$, resulting in a large frustration parameter $f = |\Theta_{CW}|/T_N \gtrsim 13$. Employing a combination of density functional theory and microscopic model simulations, we address the minimal model for Ba_2CeIrO_6 and its phase diagram. The system shows a particularly high degree of frustration, since the geometric frustration of antiferromagnetic nearest-neighbor Heisenberg exchange on the fcc lattice is augmented by next-nearest-neighbor Heisenberg coupling, yielding a wide window of a quantum spin liquid ground state. However, an antiferromagnetic Kitaev-type bond-directional exchange is found to *counteract* this geometric frustration and turns out to be instrumental in stabilizing long-range magnetic order—in contrast to the common wisdom that Kitaev

 ©2019 American Physical Society

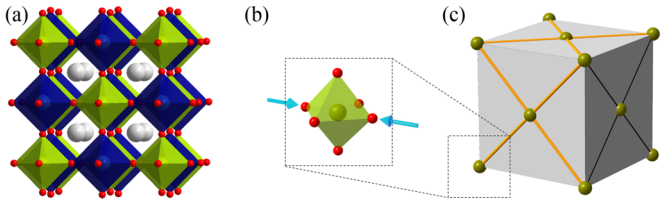

FIG. 1. (a) Cubic double-perovskite structure as observed in x-ray diffraction. Small green (large blue) octahedra are centered around the Ir^{4+} (Ce^{4+}) sites. Light gray (red) spheres depict Ba^{2+} (O^{2-}) ions. Each Ir moment is coupled to 12 nearest neighbors [orange and black lines in (c)] and to six next-nearest neighbors [along the edges of the cube in (c)], enhancing the frustration. Our RIXS data reveal local distortions from cubic symmetry. Assuming that the distortion is tetragonal, as schematically illustrated in (b), we find a massive bond-dependent variation of the nearest-neighbor exchange constants between Ir moments as depicted in (c), where couplings indicated in orange and black have different strength, reducing the frustration.

interactions in $j = 1/2$ compounds enhance frustration and induce spin liquid physics.

It is also common wisdom that the $j = 1/2$ wave function does not show orbital degeneracy and hence is not Jahn-Teller active. Commonly, this is interpreted as a protection of $j = 1/2$ physics against lattice distortions, and small deviations from cubic symmetry with the concomitant change of the wave function are typically neglected. We challenge this point of view and provide theoretical evidence for a strong magnetoelastic effect. Our theoretical analysis shows that even small deviations from the $j = 1/2$ wave function, associated with small lattice distortions, yield a massive bond-dependent variation of the nearest-neighbor exchange constants, as illustrated in Fig. 1(c), effectively lifting the strong magnetic frustration. This dramatic magnetoelastic coupling is of general importance in the quest for exotic spin liquids based on $j = 1/2$ compounds.

II. SYNTHESIS AND STRUCTURE

Single crystals of Ba_2CeIrO_6 of about $1mm^3$ size were grown by melt solution growth (see Appendix A). X-ray diffraction shows a well ordered double perovskite with Ce-Ir order as illustrated in Fig. 1(a). The cation order can be explained by the notably different bond lengths of 2.20 Å for Ce-O and 2.04 Å for Ir-O. For $5d^5$ Ir^{4+}, the formation of ideal $j = 1/2$ moments requires a cubic crystal field. Thus far, deviations from cubic symmetry were reported for all $5d^5$ iridate compounds [2,13], as discussed in more detail in the section on RIXS below.

For Ba_2CeIrO_6, our powder diffraction peaks—measured using a Stoe Stadi MP 198 powder diffractometer—are very well described in the cubic space group $Fm\bar{3}m$ with a lattice constant of 8.47 Å at 300 K. However, we find a clear broadening of Bragg peaks in particular for large diffraction angles $2\theta > 80°$. Such broadened Bragg peaks may explain a previous claim of tiny ($< 0.2\%$) monoclinic distortions of the metric in polycrystalline Ba_2CeIrO_6 [20]. Note that the issue of cubic or noncubic symmetry is often discussed controversially in double perovskites, for instance for the closely related Ba_2PrIrO_6 [20,21].

TABLE I. Results of structure refinements with single-crystal x-ray data obtained at room temperature and 100 K. In space group $Fm\bar{3}m$ Ba occupies an 8*c* site at (1/4,1/4,1/4), Ce a 4*a* site at (0,0,0), Ir a 4*b* site at (0,0,1/2), and O a 24*e* site at (*x*,0,0). Thermal parameters are given in 10^{-5} Å^2, and only the O parameters are anisotropic. The weighted *R* values for the structure factor amount to 4.22% and 3.96% at 300 K and 100 K, respectively, and refining occupations reduces them to 2.57% and 3.11%, respectively. The occupation of Ba and O was fixed. For the occupation of Ce and Ir we find 99.6% (99.1%) and 94.6% (95.0%) at 300 K (100 K), respectively, with an uncertainty of roughly 1%.

T(K)	U(Ba)	U(Ce)	U(Ir)	x(O)	U_{11}(O)	U_{22}(O)
300	1299(8)	740(8)	475(6)	0.2592(3)	1230(140)	2390(110)
100	1087(13)	738(18)	585(12)	0.2590(7)	1100(300)	2200(200)

To resolve this issue, we collected single-crystal x-ray diffraction data. Our results strongly support a cubic structure of Ba_2CeIrO_6. We employed a Bruker X8 Apex diffractometer, a sample with octahedral shape ({111} faces), and a distance to the center of 12.5 μm. At room temperature (100 K) 32921 (13274) Bragg reflection intensities were recorded, yielding 198 (205) independent reflections in space group $Fm\bar{3}m$. The single-crystal data do not yield any evidence for significant superstructure reflections with respect to $Fm\bar{3}m$, neither at room temperature nor at 100 K (see Appendix A). From this and the description of the powder diffraction pattern with the cubic lattice we must conclude that the average structure of Ba_2CeIrO_6 is cubic.

However, the atomic displacement parameters shown in Table I provide evidence for local distortions since they are (i) larger than expected for a purely dynamical displacement, (ii) very similar at 300 K and 100 K, and (iii) similar for the heavy Ba ions and the lighter O ions. The large values observed for O perpendicular to its bond at room temperature reflect the general instability of a perovskite against tilting. But the small difference in the room-temperature and 100 K displacement values in general indicates some local distortions. Moreover, a normal dynamical effect cannot explain the fact that the atomic displacement parameter of the heavy Ba is of the same magnitude (a root mean square displacement of the order of 0.1 Å) as the one of the much lighter O. Fits of the data in space groups with the same translation lattice but reduced symmetry do not yield significant improvement. However, a split model in which the Ba ions are statistically distributed over sites slightly displaced by δ_{Ba} against the cubic (0.25,0.25,0.25) position results in $\delta_{Ba} = 0.13(1)$ Å and 0.14(2) Å at 300 K and 100 K, respectively. The statistical character may be related to the existence of about 5% of vacancies on the Ir sites.

One example for structural distortions that were first sensed by enlarged atomic displacement parameters is KH_2PO_4, a prototype ferroelectric material that exhibits highly enlarged atomic displacement parameters above its ferroelectric transition of order-disorder character [22]. Another example is $La_{1.85}Sr_{0.15}CuO_4$, in which enhanced atomic displacement

factors are observed in samples which do not show long-range tilt order [23]. In Ba_2CeIrO_6, the presence of local distortions from cubic symmetry is supported by our RIXS data, see below. This can be reconciled with the observation of a global cubic structure in x-ray diffraction by assuming a negligible correlation length of the distortions. We conclude that Ba_2CeIrO_6 is cubic on average but exhibits small local distortions.

This result is in contrast to an earlier report on a monoclinic structure of Ba_2CeIrO_6 in Ref. [20] which was based on powder data and a tiny monoclinic distortion of the metric ($a/b = 1.0016$ [20]) that can result from the broadening of Bragg peaks. Combining the typical rotation of octahedra in the $GdFeO_3$ structure type of a perovskite ABO_3 with the doubling of the unit cell in the double perovskite results in a monoclinic distortion, $P2_1/c$. One may examine the possible instability of Ba_2CeIrO_6 by calculating the Goldschmidt tolerance factor for perovskites

$$t_p = \frac{r_A + r_O}{\sqrt{2}(r_B + r_O)} \tag{1}$$

with the ionic radii r_i. For an ideal cubic perovskite, $t_p = 1$. For the hypothetic perovskites $BaIrO_3$ and $BaCeO_3$ this yields $t_p = 1.06$ and 0.94 not indicating sizable bond-length mismatch. The same analysis for distorted Sr_2CeIrO_6 yields $t_p = 0.90$ and 0.80. Alternatively, one may consider the tolerance factor t_{dp} for an ordered double perovskite $A_2BB'O_6$ with r_B in Eq. (1) to be replaced by $(r_B + r_{B'})/2$. A monoclinic structure is favored for $t_{dp} \leqslant 0.96$ while values close to 1 point towards a cubic structure [24]. For Ba_2CeIrO_6, one finds $t_{dp} = 0.991$, supporting a cubic structure.

III. MAGNETIC SUSCEPTIBILITY

To explore the magnetism of the local moments in Ba_2CeIrO_6 we measured the magnetization and the magnetic susceptibility $\chi(T)$. We used an assembly of 20 small single crystals in order to enhance the magnetic signal. The crystals were not aligned because an isotropic magnetic susceptibility is expected in the paramagnetic phase of the (global) cubic structure. As shown in the lower inset of Fig. 2, we observe a field-linear magnetization. The main panel of Fig. 2 shows $\chi(T)$. Its high-temperature behavior essentially follows a Curie-Weiss behavior from 300 K down to about $T_N = 14$ K, where a distinct drop in $\chi(T)$ signals antiferromagnetic ordering. For the quantitative analysis we use

$$\chi(T) = N_A \frac{\mu_{\text{eff}}^2}{3k_B(T - \Theta_{\text{CW}})} + \chi_0 \,, \tag{2}$$

where N_A and k_B denote Avogadro's and Boltzmann's constant, respectively, Θ_{CW} is the Curie-Weiss temperature, and the constant $\chi_0 = \chi_{\text{dia}} + \chi_{vV}$ represents core diamagnetism $\chi_{\text{dia}} \simeq -1.7 \times 10^{-4}$ emu/mol and van Vleck paramagnetism $\chi_{vV} > 0$, which are expected to be of the same order of magnitude [25]. A fit based on Eq. (2) describes the data above T_N very well, see red line in Fig. 2, and yields the parameters $\chi_0 = 1.2 \times 10^{-4}$ emu/mol, $\mu_{\text{eff}} = 1.41\ \mu_B$, and $\Theta_{\text{CW}} = -184$ K. Very similar values, $\mu_{\text{eff}} = 1.3\ \mu_B$ and $\Theta_{\text{CW}} = -177$ K, were reported in a previous study on polycrystalline Ba_2CeIrO_6 [20]. To estimate the reliability of our result, we

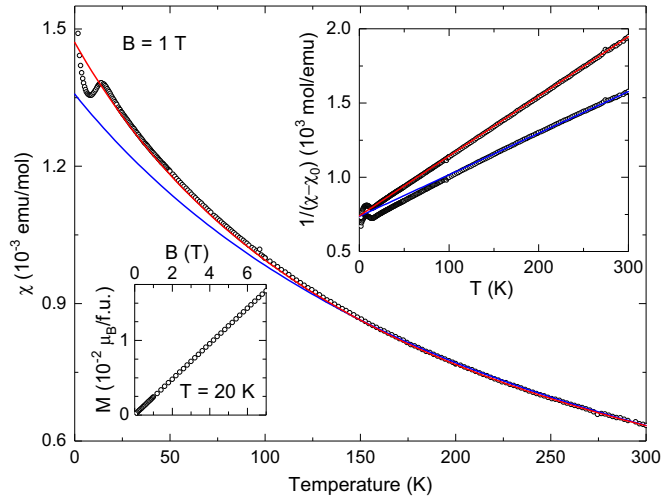

FIG. 2. Magnetic susceptibility of Ba_2CeIrO_6, measured on an assembly of 20 single crystals with 21mg total mass in a field of 1T. The red curve denotes a Curie-Weiss fit which yields $\chi_0 = 1.2 \times 10^{-4}$ emu/mol, while the blue curve corresponds to a fit restricted to $\chi_0 = 0$. The upper inset shows the same data plotted as $1/(\chi - \chi_0)$. The lower inset displays the linear field dependence of the magnetization, using $T = 20$ K as a representative example.

compare with a fit assuming $\chi_0 = 0$, which shows Curie-Weiss behavior above about 120 K (blue line in Fig. 2), $\mu_{\text{eff}} = 1.69\ \mu_B$ and $\Theta_{\text{CW}} = -263$ K, i.e., an even larger value of $|\Theta_{\text{CW}}|$. Thus, both fits result in an effective magnetic moment that is moderately reduced from $\mu_{\text{eff}} = 1.73\mu_B$ expected for $j = 1/2$ moments in an ideal cubic crystal field [26] and indicate substantial frustration with a frustration parameter $f = |\Theta_{\text{CW}}|/T_N > 13$.

IV. RIXS

Ba_2CeIrO_6 indeed realizes nearly ideal local $j = 1/2$ moments, which can be inferred from our RIXS results. In cubic symmetry, a single $5d^5$ Ir^{4+} site with a t_{2g}^5 configuration is expected to show a local $j = 1/2$ ground state and a $j = 3/2$ excited state, the so-called spin-orbit exciton, at 1.5λ with $\lambda = 0.4$–0.5 eV. The effect of a noncubic crystal field is described by the single-site Hamiltonian

$$H_{\text{single}} = \lambda\, \vec{S} \cdot \vec{L} + \Delta_{\text{CF}} L_z^2 \,, \tag{3}$$

which shows a crystal-field splitting of the $j = 3/2$ quartet and a mixing of $j = 1/2$ and $3/2$ wave functions in the ground state, $|0\rangle = \alpha|\frac{1}{2}, \frac{1}{2}\rangle + \beta|\frac{3}{2}, \frac{1}{2}\rangle$ in the $|j, j_z\rangle$ basis. With $\alpha = (\sin\theta + \sqrt{2}\cos\theta)/\sqrt{3}$ and $\tan 2\theta = \sqrt{8}/(1 - 2\Delta_{\text{CF}}/\lambda)$ [5] we can readily infer the ground state wave function by measuring Δ_{CF}.

To do so, we performed RIXS measurements at the Ir L_3 edge, the most sensitive probe for the corresponding intra-t_{2g} excitations. For $\Delta_{\text{CF}}/\lambda \ll 1$, the experimentally observed peak splitting amounts to $\Delta_{\text{exp}} = \frac{2}{3}\Delta_{\text{CF}}$. Thus far, all experimental results on the spin-orbit exciton in iridates show a finite noncubic crystal-field splitting [2,13,27–31]. The smallest values $\Delta_{\text{exp}} = 0.11$–$0.14$ eV were reported for Rb_2IrF_6, Na_2IrO_3, and Sr_2IrO_4 [27–29]. In Rb_2IrF_6, F-Ir-F bond angles

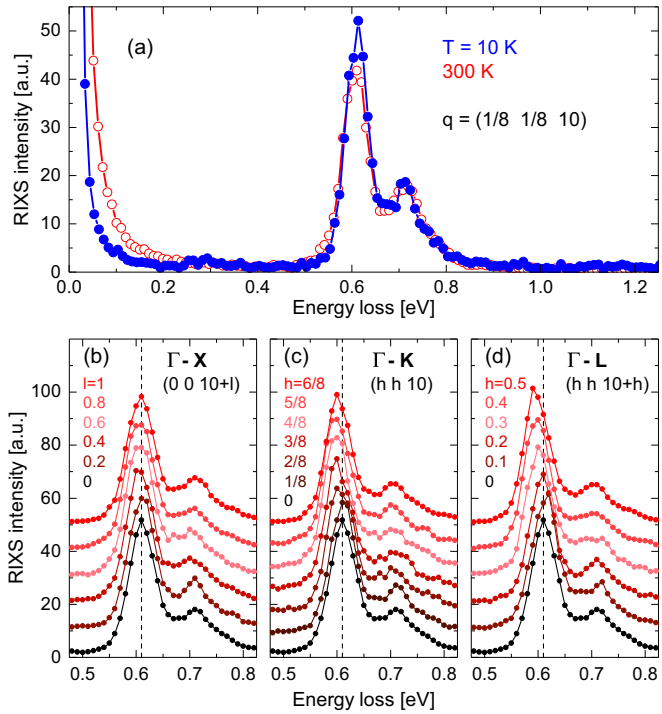

FIG. 3. RIXS data of Ba_2CeIrO_6. (a) RIXS peaks at 0.61 eV and 0.71 eV correspond to excitations to $j = 3/2$ states which are split by a noncubic crystal field. Data at 300 K show a slightly enhanced peak width but the same splitting as at 10 K. (b)–(d) Dispersion along high-symmetry directions at 10 K. The dashed line denotes the peak energy at the Γ point, 0.61 eV. The largest dispersion is observed from Γ to L, i.e., along $(h\ h\ h)$. All RIXS spectra were measured in the Brillouin zone around (0 0 10) to achieve a scattering angle 2θ close to 90° which suppresses the contribution of the elastic line at zero energy loss.

vary from 87° to 93° [29], while Sr_2IrO_4 shows distorted IrO_6 octahedra with Ir-O bond lengths of 1.98–2.06 Å and Ir-O-Ir bond angles of 157° [32]. Despite the substantial distortions, these compounds are widely accepted as realizations of the $j = 1/2$ scenario. In contrast, strong deviations from the $j = 1/2$ model are reported for Sr_3CuIrO_6 and $CaIrO_3$ with $\Delta_{exp} = 0.23$ eV and 0.6 eV, respectively [30,31].

For Ba_2CeIrO_6, we measured RIXS data on a polished (0 0 1) surface at the ID20 beamline at ESRF using an incident energy of 11.215 keV with an overall resolution of 25 meV [33,34]. The incident photons were π polarized. Our data offer a textbook example of the spin-orbit exciton by showing two narrow RIXS peaks on a negligible background, see Fig. 3. Similar RIXS spectra with a slightly larger peak splitting were reported for Rb_2IrF_6 [29] and $Ba_3Ti_{2.7}Ir_{0.3}O_9$ [35], two compounds with well separated Ir^{4+} ions. In comparison, $5d^5$ iridates with stronger hopping such as Na_2IrO_3 and Sr_2IrO_4 show more complex RIXS features [27,28] with, e.g., further peaks, broader linewidths, and/or a continuum contribution. In Ba_2CeIrO_6, the peaks are located at about 0.61 eV and 0.71 eV, both at 10 K and at 300 K. The observation of *two* peaks signals noncubic local distortions in agreement with our analysis of the x-ray diffraction data. A fit using two peaks with the Pearson VII line shape [36] that mimics a convolution of an intrinsic Lorentzian line shape and a Gaussian profile with the experimental resolution yields a splitting $\Delta_{exp} = (100 \pm 4)$ meV, the smallest splitting reported thus far in L edge RIXS for the spin-orbit exciton in iridates [27–31,35]. The peak values of 0.61 eV and 0.71 eV allow for two different solutions of Eq. (3) with $\lambda = 0.43$ eV and $\Delta_{CF} = 0.17$ eV or -0.15 eV, which correspond to elongation or compression, respectively. This results in a ground-state wave function

$$|0\rangle = 0.991\left|\frac{1}{2}, \frac{1}{2}\right\rangle - 0.130\left|\frac{3}{2}, \frac{1}{2}\right\rangle \tag{4}$$

in the $|j, j_z\rangle$ basis for elongation, while for compression the coefficients are 0.995 and 0.100, respectively. Note that both solutions deviate by less than 1% from the ideal $j = 1/2$ case.

To probe the intersite hopping interactions, we have measured the dispersion via RIXS for $\mathbf{q}$ along different high-symmetry directions. Data along Γ-K and Γ-L paths reveal a finite dispersion of up to 15–20 meV, while peak energies are nearly independent of $\mathbf{q}$ along Γ-X, see the lower panels of Fig. 3. The corresponding delocalization of the $j = 3/2$ excited state is a clear signature of microscopic hopping processes and intersite interactions that are closely related to the magnetic exchange interactions between localized $j = 1/2$ moments [28,37]. Roughly, this common microscopic origin is reflected in the common energy scale of 15–20 meV of the spin-orbit exciton dispersion and the Curie-Weiss temperature, which also is a measure of the size of magnetic exchange interactions.

V. MICROSCOPIC MODEL

A. fcc lattice with cubic site symmetry

A symmetry analysis [38–40] of exchange interactions on the undistorted fcc lattice shows that the most general nearest-neighbor spin Hamiltonian allows for Heisenberg coupling J_1, Kitaev coupling K, and symmetric off-diagonal exchange Γ. We estimate the coupling constants using density functional theory (GGA+U+SOC) for different magnetic configurations and t/U perturbation theory for an effective tight-binding model (see Appendix B). Both approaches consistently yield an antiferromagnetic $J_1 \approx 5$–7 meV and two subdominant couplings $K \approx J_2 \approx 0.2\,J_1$, where J_2 denotes a next-nearest neighbor Heisenberg coupling. We find that $\Gamma/J_1 \lesssim 0.05$ is negligible. The corresponding Curie-Weiss temperature $\Theta_{CW} = -(3J_1 + K + 3J_2/2) \approx -200$ K to -280 K agrees with the experimental $\chi(T)$; see Fig. 2. Note that we find an antiferromagnetic Kitaev coupling, in contrast to the ferromagnetic ones inferred for the honeycomb-based iridates and α-$RuCl_3$ [41]. The ferromagnetic Kitaev coupling of the latter arises from Hund's coupling in the virtually excited intermediate state with two holes on the same site, favoring parallel hole spins. For the honeycomb materials with a 90° Ir-O-Ir exchange path, this translates into a ferromagnetic coupling of $j = 1/2$ pseudospins. In Ba_2CeIrO_6, exchange proceeds via an Ir-O-O-Ir path with a different combination of orbitals in the virtual state. Again, Hund's coupling favors parallel spins of the two holes, but for the relevant orbitals this translates to *antiferromagnetic* coupling of $j = 1/2$ pseudospins (see Appendix C).

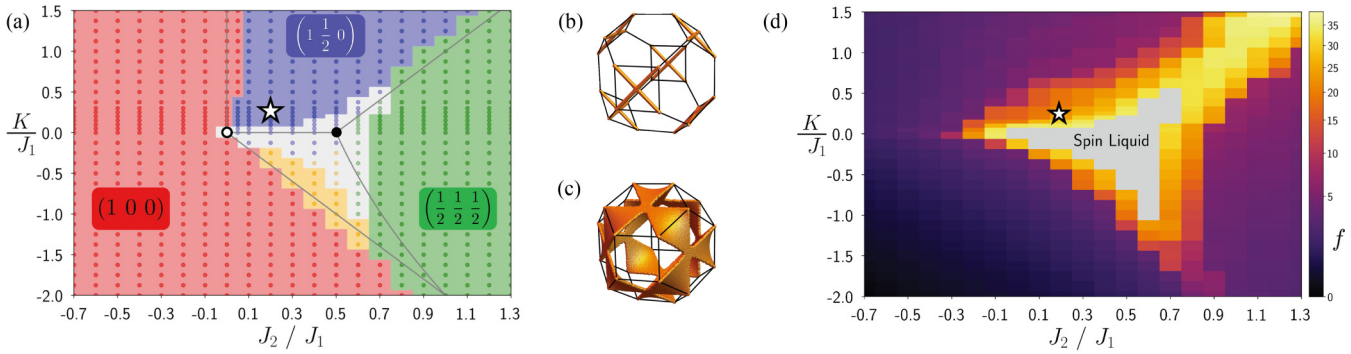

FIG. 4. (a) Phase diagram for the J_1-J_2-K model. We find ordered phases with ordering wave vectors (100) (red), $(\frac{1}{2}\frac{1}{2}\frac{1}{2})$ (green), and $(1\frac{1}{2}0)$ (blue), an incommensurate spiral phase (yellow) whose ordering wave vector continuously varies within the phase, and a spin liquid regime (gray). The lines indicate the phase boundaries of the classical model for comparison. White and black circles mark high-degeneracy points of the classical model (see text), their corresponding sets of **q** vectors are shown in (b) and (c), respectively. The star indicates the parameter set obtained for Ba_2CeIrO_6. (d) The frustration parameter $f = |\Theta_{CW}|/T_N$ shows the suppression of ordering tendencies caused by the interplay of geometric and exchange frustration. Gray: spin liquid regime.

To study the competition of geometric and exchange frustration, we explore the minimal microscopic model

$$\mathcal{H} = J_1 \sum_{\langle i,j\rangle} \vec{\mathcal{S}}_i \cdot \vec{\mathcal{S}}_j + K \sum_{\langle i,j\rangle_\gamma} \mathcal{S}_i^\gamma \mathcal{S}_j^\gamma + J_2 \sum_{\langle\langle i,j\rangle\rangle} \vec{\mathcal{S}}_i \cdot \vec{\mathcal{S}}_j, \quad (5)$$

where $\langle i, j\rangle_\gamma$ denotes nearest-neighbor pairs in the plane perpendicular to axis γ $(= x, y, z)$, $\langle\langle i, j\rangle\rangle$ runs over next-nearest-neighbor pairs, and the spin operators $\vec{\mathcal{S}}$ refer to $j = 1/2$ moments. We have calculated its rich phase diagram using a pseudofermion functional renormalization group (pf-FRG) approach [42]. This numerical scheme combines elements from $1/S$ expansion [43] and $1/N$ expansion [44,45], allowing it to capture both magnetic order and spin-liquid ground states. There are four magnetically ordered phases, one of them showing incommensurate spiral order, see Fig. 4(a). These phases can be readily understood in the classical limit of model (5) via a Luttinger-Tisza approach [46,47], with the classical phase boundaries also indicated in Fig. 4(a). The quantum model additionally exhibits a spin-liquid phase with no magnetic order. Its origin is revealed by two points of special interest in the classical model, see white and black circles in Fig. 4(a): (i) $J_2 = K = 0$, the fcc nearest-neighbor Heisenberg antiferromagnet. It exhibits a degenerate manifold of coplanar spin spiral ground states [48]. The corresponding set of **q** vectors is shown in Fig. 4(b). (ii) $J_2 = J_1/2$, $K = 0$, where three ordered phases meet in the classical model. This point features an even larger set of degenerate coplanar spin-spiral ground states, depicted by the *surface* of **q** vectors in Fig. 4(c). The presence of a considerable (but still subextensive) manifold of (nearly) degenerate low-energy states appears to give rise to an extended spin liquid regime in the quantum model, centered around the classical high-degeneracy point [49].

To further investigate the interplay of geometric and exchange frustration, we calculate [50] the dimensionless frustration parameter $f = |\Theta_{CW}|/T_N$, see Fig. 4(d), using estimates of Θ_{CW} and T_N obtained from fits of the magnetic susceptibility numerically obtained by FRG calculations. The frustration parameter diverges in the spin liquid regime due to the absence of finite-temperature order. Furthermore, f is particularly large along the phase boundary between the $(1\frac{1}{2}0)$ and $(\frac{1}{2}\frac{1}{2}\frac{1}{2})$ phases, where both J_2 and K are substantial and antiferromagnetic. This boosts $|\Theta_{CW}|$ while T_N is small close to the phase boundary. Close to the spin-liquid regime for the parameter set estimated for Ba_2CeIrO_6 [cf. star in Fig. 4(d)], we also find large values of f. However, moving away from the spin-liquid regime the frustration is quickly reduced with increasing strength of the Kitaev coupling. This is consistent with a previous classical Monte Carlo study [38,39], although such a classical analysis by itself is not reliable in the deep quantum limit of $j = 1/2$. Our results show that the Kitaev coupling, in competition with the geometric frustration of the Heisenberg exchange, indeed induces magnetic order for the system at hand – in striking contrast to a number of $j = 1/2$ materials where the Kitaev coupling is primarily considered a source of frustration [2,13].

B. Distortions

The strong frustration in Ba_2CeIrO_6 boosts the importance of magnetoelastic coupling. We find theoretically that even small local distortions severely affect the exchange couplings, although the ground state wave function remains close to the $j = 1/2$ limit, see Eq. (4). The precise character of the local distortions cannot be determined from our x-ray diffraction results, which show global cubic symmetry. A putative tetragonal distortion of strength Δ_{CF} gives rise to a strong spatial anisotropy, which can be rationalized as follows. Focusing, e.g., on the dominant contribution to exchange within the xy plane, we find J_1^{xy} to depend quadratically on the occupation probability of the xy orbital. Comparing cubic $\Delta_{CF} = 0$ with the distorted case $\Delta_{CF}/\lambda \approx 0.4$ derived above, the xy occupation is strongly enhanced from 1/3 to 0.46 and as a result the nearest-neighbor Heisenberg exchange J_1^{xy} increases by about a factor of two, which corresponds to a dramatic magnetoelastic effect. In particular, $\Delta_{CF} > 0$ strengthens (weakens) J_1, J_2, and K in the xy plane (yz and xz planes), while $\Delta_{CF} < 0$ has the reverse effect. This strong spatial anisotropy of the couplings is sketched in Fig. 1(c). Note that a change of the xy occupation $\sin^2\theta$ has a much more pronounced effect on the exchange, $J_1 \propto \sin^4\theta$, than

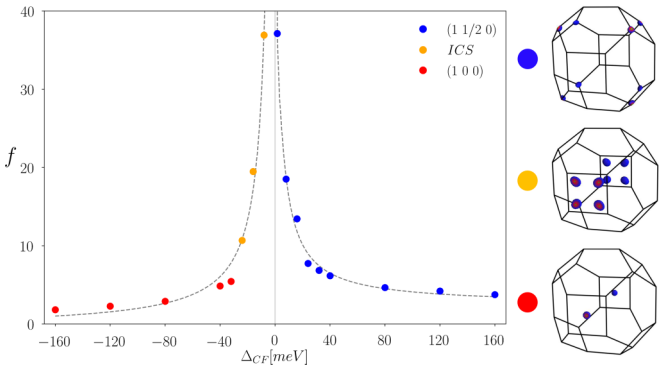

FIG. 5. Frustration parameter as a function of the tetragonal distortion Δ_{CF}. Colors indicate different types of magnetic order, with respective structure factors, calculated using the pf-FRG scheme, shown to the right. The abbreviation ICS denotes the incommensurate spiral phase.

on the coefficient $\alpha = \sqrt{1/3}\sin\theta + \sqrt{2/3}\sqrt{1-\sin^2\theta}$ of the $|\frac{1}{2},\frac{1}{2}\rangle$ contribution to the ground state wave function. The comparably small change of α indicates a small deviation from a cubic charge distribution and a concomitant small energy cost for lattice distortions, while the larger change of J_1 and in particular its spatial anisotropy yield a significant gain of magnetic energy, particularly in the presence of frustration.

To analyze the effect of a *global* tetragonal lattice distortion, we have simulated a variant of the J_1-J_2-K model, cf. Eq. (5), with anisotropic coupling strengths, enhancing/reducing the couplings as described above and illustrated in Fig. 1(c). Specifically, we have modeled the dependence of the coupling parameters on the distortion Δ_{CF} as

$$J_1 \to \begin{cases} J_1 + \delta J(\Delta_{\mathrm{CF}}), & xy \text{ plane}, \\ J_1 - \delta J(\Delta_{\mathrm{CF}}), & yz,\ xz \text{ planes}, \end{cases} \tag{6}$$

and, analogously, for J_2 and K. For $\Delta_{\mathrm{CF}} = 0$ this corresponds to the parameter set indicated by a star in Fig. 4(d), i.e., $J_2 = K = 0.2J_1$, while for $\Delta_{\mathrm{CF}} = \Delta_{\mathrm{CF}}^{\max} = 160$ meV we have the enhanced xy couplings $J_1^{xy} = 2J_1$, $J_2^{xy} = 1.2J_2$, and $K^{xy} = 1.2K$ for simultaneously reduced parameters $J_1^{xz,yz} = 0.6J_1$, $J_2^{xz,yz} = 0.7J_2$, and $K^{xz,yz} = 0.8K$ in the xz and yz plane. The function $\delta J(\Delta_{\mathrm{CF}})$ is well approximated as a linear interpolation

$$\delta J(\Delta_{\mathrm{CF}}) = \frac{\Delta_{\mathrm{CF}}}{\Delta_{\mathrm{CF}}^{\max}}\left(J\left(\Delta_{\mathrm{CF}}^{\max}\right) - J(\Delta_{\mathrm{CF}} = 0)\right). \tag{7}$$

Results for pf-FRG calculations are summarized in Fig. 5 showing the frustration parameter $f = |\Theta_{\mathrm{CW}}|/T_{\mathrm{N}}$ as a function of the distortion Δ_{CF}. As clearly visible, the frustration is strongly suppressed by the distortions, it quickly approaches a nonfrustrated regime $f \lesssim 5$ for distortions of the order of $|\Delta_{\mathrm{CF}}| \approx 40$ meV, independent of the sign of the distortion. Additionally, the data indicate a potential change of magnetic order, for instance to (100) order, depending on the sign and the strength of Δ_{CF}. These results agree with the small $f \lesssim 2$ reported for the globally distorted monoclinic $5d^5$ double perovskites La_2ZnIrO_6 and La_2MgIrO_6 [39]. However, this result for a *global* distortion is significantly smaller than the value of $f > 13$ measured in Ba_2CeIrO_6. This suggests that the statistical distribution of *local* distortions along different tetragonal axes, in contrast to a global distortion, is important in order to recover the experimentally observed large frustration.

The existence of a weak (but unavoidable) magnetoelastic effect was recently discussed for Sr_2IrO_4 [51]. The strong effect of the magnetoelastic coupling in Ba_2CeIrO_6, however, is due to an additional mechanism arising from an interplay of distortions and magnetic frustration, which is not present in Sr_2IrO_4, but will be relevant, e.g., in tetragonal bilayer $Sr_3Ir_2O_7$ and in the 3D honeycomb iridates.

VI. CONCLUSIONS

The spin-orbit entangled $j = 1/2$ wave function has proved to be a versatile source for novel states of quantum matter. Its experimental realization in the double perovskite Ba_2CeIrO_6 deviates less than 1% from the ideal theoretical scenario for a cubic system and is one of the most pristine $j = 1/2$ incarnations reported so far in the literature. Combining structural analysis, magnetic susceptibility measurements, and RIXS with *ab initio* and functional renormalization group calculations for the obtained microscopic model Hamiltonian we find that the collective magnetism of this fcc compound is governed by a competition of geometrical frustration, Kitaev-type bond-directional exchange, and magnetoelastic coupling. In striking contrast to the honeycomb-based Kitaev materials, the Kitaev exchange is antiferromagnetic and in fact stabilizes long-range magnetic order in proximity to a spin liquid phase. Importantly, the exchange couplings turn out to be highly sensitive to small deviations from cubic symmetry, giving rise to a dramatic magnetoelastic coupling. This should be contrasted with the common notion that $j = 1/2$ moments are not Jahn-Teller active, as the orbital degeneracy is lifted by spin-orbit coupling. The strong magnetoelastic coupling resurrects the prominent role of lattice distortions on the low-energy properties of $j = 1/2$ compounds.

Note added. Recently, Aczel *et al.* reported similar experimental results on polycrystalline samples of Ba_2CeIrO_6 [52]. They find (100) magnetic order, in agreement with our calculations for negative Δ_{CF}. Furthermore, Khan *et al.* [53] reported on the realization of cubic site symmetry in K_2IrCl_6 based on x-ray diffraction data; a spectroscopic proof of this claim is still missing.

ACKNOWLEDGMENTS

We acknowledge funding from the Deutsche Forschungsgemeinschaft (DFG, German Research Foundation) – Project numbers 277146847 and 247310070 – CRC 1238 (projects A02, B01, B02, B03, C02, C03) and CRC 1143 (project A05), respectively. M.H. acknowledges partial funding by the Knut and Alice Wallenberg Foundation and the Swedish Research Council. A.P. acknowledges support from NSERC of Canada and the Canadian Institute for Advanced Research, and the support and hospitality of the University of Cologne. The numerical simulations were performed on the JURECA booster at FZ Jülich and the CHEOPS cluster at RRZK Cologne. DFT calculations were supported by the Russian Science Foundation via project 17-12-01207.

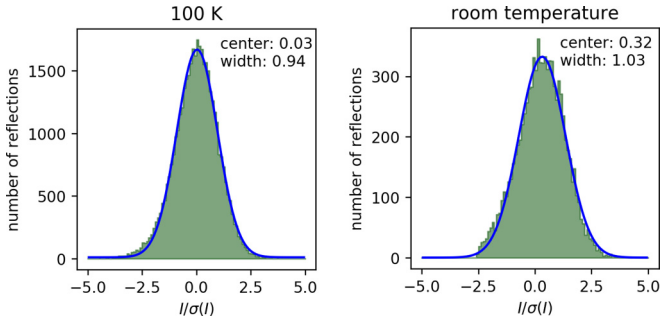

FIG. 6. Results of single-crystal x-ray diffraction. Histogram of the intensities of peaks forbidden in $Fm\bar{3}m$ divided by their respective error bars. Left: $T = 100$ K. Right: room temperature. Blue lines: Gaussian fits. Note that negative values of the intensities arise due to the subtraction of a small overall background. The data do not yield any significant evidence for reflections of a noncubic structure.

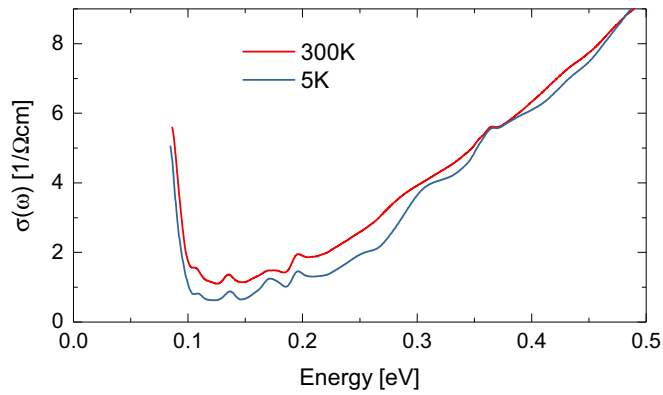

FIG. 7. Optical conductivity of Ba_2CeIrO_6, showing the onset of excitations across the Mott gap.

APPENDIX A: SINGLE-CRYSTAL GROWTH AND CHARACTERIZATION

We have grown single crystals of Ba_2CeIrO_6 by melt solution growth using $BaCl_2$ as melt solvent and $BaCO_3$ (Merck, p.a.), IrO_2 (Chempur, 99.9%), and CeO_2 (Auer Remy, 99.9%) as educts for the crystals. Due to the moderate solubility of metal oxides in halide melts [57], a ratio flux/crystal of 15/1 was used to achieve sufficient dissolution of the oxides. The crucible was sealed with a lid to prevent evaporation of $BaCl_2$ from the melt solution. Within three weeks single crystals of about 1mm^3 size were obtained. The black single crystals were separated from the flux by dissolving the flux in deionized water and analyzed by energy-dispersive x-ray scattering.

Our single-crystal x-ray diffraction data strongly support a cubic structure of Ba_2CeIrO_6, as explained in the main text. Figure 6 shows the distribution of the observed peak intensities I divided by their error bars $\sigma(I)$ for all reflections that are not allowed in space group $Fm\bar{3}m$. The width of the distributions is approximately 1, which is an indication for meaningful statistical errors of the intensities. Both at room temperature and at 100 K, we find a Gaussian profile peaking at a value of $I/\sigma(I)$ close to zero or much smaller than 1, i.e., the intensities of forbidden peaks are negligible within the experimental error bars.

The excellent agreement of the RIXS spectra shown in Fig. 3 with the expectations for the spin-orbit exciton provides an unambiguous fingerprint of the Ir^{4+} valence state. RIXS spectra for $5d^4$ Ir^{5+} are distinctly different, as reported for, e.g., the double perovskites Sr_2YIrO_6 and Ba_2YIrO_6 [58,59]. In Ba_2CeIrO_6, the Ir^{4+} valence means that also the Ce ions are tetravalent, as claimed before [20] based on the dependence of the lattice parameters on the ionic radius of the lanthanide ions Ln in Ba_2LnIrO_6.

The Mott-insulating character of Ba_2CeIrO_6 is demonstrated by the very low value of the optical conductivity in the mid-infrared range, $\sigma_1(\omega) \approx 1\ (\Omega\text{cm})^{-1}$, see Fig. 7. Using a Bruker IFS 66/v Fourier-transform infrared spectrometer, we measured the transmittance on a single crystal with a thickness of (30 ± 5) μm. On the low-frequency side, the accessible frequency range is cut off by strong phonon absorption suppressing the transmittance. The steep edge in $\sigma_1(\omega)$ at about 0.1 eV corresponds to the upper limit for single phonon absorption, while the weak features up to about 0.2 eV can be attributed to multiphonon absorption. On the high-frequency side, the transmittance is suppressed by electron-hole excitations across the gap, giving rise to the increase of $\sigma_1(\omega)$ above about 0.2 eV.

APPENDIX B: DERIVATION OF MICROSCOPIC MODEL

Ab initio calculations.– In order to calculate Heisenberg-type and Kitaev-type exchange constants, we used the projector augmented-wave (PAW) method [60] as realized in the pseudopotential VASP code [61]. The exchange-correlation potential was chosen in the form proposed by Perdew, Burke, and Ernzerhof [62]. Electronic correlations and spin-orbit coupling were considered in the framework of the GGA+U+SOC formalism [63] with $U - J_H = 2.0$ eV [11], where U and J_H denote the on-site Coulomb repulsion and intra-atomic Hund's exchange, respectively. The integration was performed on a $7 \times 7 \times 7$ mesh of the Brillouin zone. We calculated total energies of three magnetic configurations (FM, AFM type I and type II) to extract nearest and next-nearest neighbor exchange constants J_1 and J_2. The Kitaev coupling K was computed via the difference of the total energies of two AFM type I configurations with spins pointing along a and c, respectively.

Perturbative approach. For the perturbative calculation of exchange couplings, we use one-hole and two-hole eigenstates and energies obtained by numerical diagonalization of the single-site Hamiltonian

$$H_{\text{site}} = -i\frac{\lambda}{2}\sum_{\ell mn}\epsilon_{\ell mn} d^\dagger_{\ell\alpha} d_{m\beta}\sigma^n_{\alpha\beta} + \frac{U}{2}n^2_{\text{tot}} - \frac{5J_H}{2}\sum_{\ell<\ell'} n_\ell n_{\ell'} - 2J_H\sum_{\ell<\ell'}\vec{S}_\ell\cdot\vec{S}_{\ell'} + J_H\sum_{\ell\neq\ell'} d^\dagger_{\ell\uparrow}d^\dagger_{\ell\downarrow}d_{\ell'\downarrow}d_{\ell'\uparrow}, \quad \text{(B1)}$$

with $\lambda = 0.43$ eV deduced from our RIXS data, Hund's coupling $J_H = 0.25$ eV [58] and $U = 2.25$ eV as a typical estimate for the Hubbard repulsion (which leads to $U - J_H = 2.0$ eV as in the *ab initio* calculations). For the inter-site Hamiltonian, we use $H_{\text{hop}} = \sum_{\langle i,j\rangle,\sigma}\mathbf{d}^\dagger_{i\sigma}\cdot\mathbf{T}_{ij}\cdot\mathbf{d}_{j\sigma}$, with $\mathbf{d}^\dagger$ representing the creation operators for the three t_{2g} orbitals, $(d^\dagger_{yz}, d^\dagger_{xz}, d^\dagger_{xy})$. For

the hopping amplitudes $t_{\alpha-\beta}$ between a pair of orbitals (α, β) on nearest-neighbor sites $(i, i+\hat{x}+\hat{y})$, we retain only the by far dominant one $t_{xy-xy} \approx -150$ meV, which is an order of magnitude larger than t_{xz-yz} which again is larger than $t_{xz-xz} = t_{yz-yz}$, while others vanish by symmetry. For second-neighbor pairs $(i, i+2\hat{x})$, we employ $t_{xy-xy} = t_{xz-xz} \approx 30$ meV, while other hopping amplitudes vanish by symmetry. For the cubic fcc lattice, the corresponding hopping amplitudes between all other nearest-neighbor or next-nearest neighbor pairs are determined by symmetry. To extract the two-site exchange Hamiltonian, we carry out second-order degenerate perturbation theory in t/U, evaluating matrix elements numerically using exact single-site eigenfunctions and energies. The resulting exchange Hamiltonian has dominant nearest-neighbor Heisenberg exchange interaction J_1 with subdominant Kitaev and second-neighbor Heisenberg terms as listed in the main text and a negligible $\Gamma \lesssim 0.05 J_1$ exchange term.

APPENDIX C: ANTIFERROMAGNETIC CHARACTER OF KITAEV COUPLING

The $j = 1/2$ wave function is given by

$$\left|\frac{1}{2}, \mathrm{up}\right\rangle = \frac{1}{\sqrt{3}}(|yz, \downarrow\rangle + i|xz, \downarrow\rangle + |xy, \uparrow\rangle). \tag{C1}$$

We address superexchange interactions between two sites A and B in the xy plane. For comparison, we first consider edge-sharing geometry with 90° Ir-O-Ir bonds [5] as approximately realized in the honeycomb iridates. In this case, the hopping $t^{90^\circ}_{xy-xy}$ between xy_A and xy_B via an intermediate O ligand vanishes by symmetry. There are two finite hopping contributions, between xz_A and yz_B and between yz_A and xz_B. The Heisenberg interaction vanishes due to destructive interference between these two. This destructive interference originates from the phase factor i in the $j = 1/2$ wave function, see Eq. (C1). In contrast, Kitaev exchange remains finite and is ferromagnetic. The ferromagnetic character arises from the virtual intermediate state with two holes on the same site occupying the xz and yz orbitals. The energy of this intermediate state is lower for parallel spins in xz and yz, which corresponds to parallel $j = 1/2$ pseudospins, see Eq. (C1).

The same ferromagnetic contribution to Kitaev exchange is present on the fcc lattice as well where the Ir-O-Ir hopping of edge-sharing geometry has to be replaced by Ir-O-O-Ir hopping. However, the size of this ferromagnetic contribution to Kitaev exchange is negligibly small on the fcc lattice due to the very small hopping between xz and yz orbitals. In contrast to the edge-sharing geometry discussed above, the hopping $xy_A \to xy_B$ via the two intermediate O ligands does not vanish on the fcc lattice, it is in fact the dominant hopping term within the xy plane. For parallel pseudospins $|\frac{1}{2}, \mathrm{up}\rangle_A\, |\frac{1}{2}, \mathrm{up}\rangle_B$, the configuration $|xy, \uparrow\rangle_A\, |yz, \downarrow\rangle_B$ in orbital/spin basis carries finite weight, see Eq. (C1). Hopping $xy_A \to xy_B$ then yields the doubly occupied virtual state $|xy, \uparrow\rangle_B\, |yz, \downarrow\rangle_B$, and a second hopping process $xy_B \to xy_A$ brings us back to the ground state without any spin flip. This exchange will lead to an Ising-like $S^z_A S^z_B$ term. Equivalent to the case discussed above, the lowest energy in the virtual doubly occupied state is realized for two parallel spins, $|xy, \uparrow\rangle_B\, |yz, \uparrow\rangle_B$, which for this combination of orbitals corresponds to *antiparallel* pseudospins, see Eq. (C1). As a result, pure $xy_A \to xy_B$ hopping within the xy plane in combination with Hund's coupling generates a small *antiferromagnetic* Kitaev coupling $K \propto J_1 \times J_H/U$. By symmetry, it couples the z (x, y) component of the moments for two nearest-neighbor sites within the xy (yz, zx) plane.

[1] W. Witczak-Krempa, G. Chen, Y. B. Kim, and L. Balents, Correlated quantum phenomena in the strong spin-orbit regime, Annu. Rev. Condens. Matter Phys. **5**, 57 (2014).

[2] J. G. Rau, E. Kin-Ho Lee, and H.-Y. Kee, Spin-orbit physics giving rise to novel phases in correlated systems: Iridates and related materials, Annu. Rev. Condens. Matter Phys. **7**, 195–221 (2016).

[3] G. Khaliullin, Orbital order and fluctuations in Mott insulators, Prog. Theor. Phys. Suppl. **160**, 155 (2005).

[4] G. Chen and L. Balents, Spin-orbit effects in $Na_4Ir_3O_8$: A hyper-kagome lattice antiferromagnet, Phys. Rev. B **78**, 094403 (2008).

[5] G. Jackeli and G. Khaliullin, Mott Insulators in the Strong Spin-Orbit Coupling Limit: From Heisenberg to a Quantum Compass and Kitaev Models, Phys. Rev. Lett. **102**, 017205 (2009).

[6] Y. K. Kim, O. Krupin, J. D. Denlinger, A. Bostwick, E. Rotenberg, Q. Zhao, J. F. Mitchell, J. W. Allen, and B. J. Kim, Fermi arcs in a doped pseudospin-1/2 Heisenberg antiferromagnet, Science **345**, 187 (2014).

[7] A. de la Torre, S. McKeown Walker, F. Y. Bruno, S. Riccó, Z. Wang, I. Gutierrez Lezama, G. Scheerer, G. Giriat, D. Jaccard, C. Berthod, T. K. Kim, M. Hoesch, E. C. Hunter, R. S. Perry, A. Tamai, and F. Baumberger, Collapse of the Mott Gap and Emergence of a Nodal Liquid in Lightly Doped Sr_2IrO_4, Phys. Rev. Lett. **115**, 176402 (2015).

[8] Y. Cao, Q. Wang, J. A. Waugh, T. J. Reber, H. Li, X. Zhou, S. Parham, S. R. Park, N. C. Plumb, E. Rotenberg, A. Bostwick, J. D. Denlinger, T. Qi, M. A. Hermele, G. Cao, and D. S. Dessau, Hallmarks of the Mott-metal crossover in the hole-doped pseudospin-1/2 Mott insulator Sr_2IrO_4, Nat. Commun. **7**, 11367 (2016).

[9] Y. J. Yan, M. Q. Ren, H. C. Xu, B. P. Xie, R. Tao, H. Y. Choi, N. Lee, Y. J. Choi, T. Zhang, and D. L. Feng, Electron-Doped Sr_2IrO_4: An Analogue of Hole-Doped Cuprate Superconductors Demonstrated by Scanning Tunneling Microscopy, Phys. Rev. X **5**, 041018 (2015).

[10] Y. K. Kim, N. H. Sung, J. D. Denlinger, and B. J. Kim, Observation of a d-wave gap in electron-doped Sr_2IrO_4, Nat. Phys. **12**, 37 (2016).

[11] B. J. Kim, H. Jin, S. J. Moon, J.-Y. Kim, B.-G. Park, C. S. Leem, J. Yu, T. W. Noh, C. Kim, S.-J. Oh, J.-H. Park, V. Durairaj, G. Cao, and E. Rotenberg, Novel $J_{\mathrm{eff}} = 1/2$ Mott State Induced by Relativistic Spin-Orbit Coupling in Sr_2IrO_4, Phys. Rev. Lett. **101**, 076402 (2008).

[12] B. J. Kim, H. Ohsumi, T. Komesu, S. Sakai, T. Morita, H. Takagi, and T. Arima, Phase-Sensitive Observation of a Spin-Orbital Mott State in Sr_2IrO_4, Science **323**, 1329 (2009).

[13] S. Trebst, Kitaev materials, arXiv:1701.07056.

[14] Y. Singh and P. Gegenwart, Antiferromagnetic Mott insulating state in single crystals of the honeycomb lattice material Na_2IrO_3, Phys. Rev. B **82**, 064412 (2010).

[15] Y. Singh, S. Manni, J. Reuther, T. Berlijn, R. Thomale, W. Ku, S. Trebst, and P. Gegenwart, Relevance of the Heisenberg-Kitaev Model for the Honeycomb Lattice Iridates A_2IrO_3, Phys. Rev. Lett. **108**, 127203 (2012).

[16] K. Kitagawa, T. Takayama, Y. Matsumoto, A. Kato, R. Takano, Y. Kishimoto, S. Bette, R. Dinnebier, G. Jackeli, and H. Takagi, A spin–orbital-entangled quantum liquid on a honeycomb lattice, Nature (London) **554**, 341 (2018).

[17] K. W. Plumb, J. P. Clancy, L. J. Sandilands, V. Vijay Shankar, Y. F. Hu, K. S. Burch, H.-Y. Kee, and Y.-J. Kim, α-$RuCl_3$: A spin-orbit assisted Mott insulator on a honeycomb lattice, Phys. Rev. B **90**, 041112(R) (2014).

[18] Y. Kasahara, T. Ohnishi, Y. Mizukami, O. Tanaka, S. Ma, K. Sugii, N. Kurita, H. Tanaka, J. Nasu, Y. Motome, T. Shibauchi, and Y. Matsuda, Majorana quantization and half-integer thermal quantum Hall effect in a Kitaev spin liquid, Nature (London) **559**, 227 (2018).

[19] A. Kitaev, Anyons in an exactly solved model and beyond, Ann. Phys. **321**, 2 (2006).

[20] M. Wakeshima, D. Harada, and Y. Hinatsu, Crystal structures and magnetic properties of ordered perovskites Ba_2LnIrO_6 (Ln=lanthanide), J. Mater. Chem. **10**, 419 (2000).

[21] W. Kockelmann, D. T. Adroja, A. D. Hillier, M. Wakeshima, Y. Izumiyama, Y. Hinatsu, K. S. Knight, D. Visser, and B. D. Rainford, Neutron diffraction and inelastic neutron scattering investigations of the ordered double perovskite Ba_2PrIrO_6, Physica B (Amsterdam) **378**, 543 (2006).

[22] R. J. Nelmes, Structural studies of KDP and the KDP-type transition by neutron and x-ray diffraction: 1970–1985, Ferroelectrics **71**, 87 (2001).

[23] M. Braden, M. Meven, W. Reichardt, L. Pintschovius, M. T. Fernandez-Diaz, G. Heger, F. Nakamura, and T. Fujita, Analysis of the local structure by single-crystal neutron scattering in $La_{1.85}Sr_{0.15}CuO_4$, Phys. Rev. B **63**, 140510(R) (2001).

[24] S. Vasala and M. Karppinen, $A_2B'B''O_6$ perovskites: A review, Prog. Solid State Chem. **43**, 1 (2015).

[25] $\chi_{\rm dia} \simeq -1.7 \times 10^{-4}$ emu/mol results from the tabulated values [54] for the ions in Ba_2CeIrO_6.

[26] M. Moretti Sala, S. Boseggia, D. F. McMorrow, and G. Monaco, Resonant X-Ray Scattering and the $j_{\rm eff}$=1/2 Electronic Ground State in Iridate Perovskites, Phys. Rev. Lett. **112**, 026403 (2014).

[27] H. Gretarsson, J. P. Clancy, X. Liu, J. P. Hill, E. Bozin, Y. Singh, S. Manni, P. Gegenwart, J. Kim, A. H. Said, D. Casa, T. Gog, M. H. Upton, H.-S. Kim, J. Yu, V. M. Katukuri, L. Hozoi, J. van den Brink, and Y.-J. Kim, Crystal-Field Splitting and Correlation Effect on the Electronic Structure of A_2IrO_3, Phys. Rev. Lett. **110**, 076402 (2013).

[28] J. Kim, M. Daghofer, A. H. Said, T. Gog, J. van den Brink, G. Khaliullin, and B. J. Kim, Excitonic quasiparticles in a spin-orbit Mott insulator, Nat. Commun. **5**, 4453 (2014).

[29] M. Rossi, M. Retegan, C. Giacobbe, R. Fumagalli, A. Efimenko, T. Kulka, K. Wohlfeld, A. I. Gubanov, and M. Moretti Sala, Possibility to realize spin-orbit-induced correlated physics in iridium fluorides, Phys. Rev. B **95**, 235161 (2017).

[30] X. Liu, V. M. Katukuri, L. Hozoi, W.-G. Yin, M. P. M. Dean, M. H. Upton, J. Kim, D. Casa, A. Said, T. Gog, T. F. Qi, G. Cao, A. M. Tsvelik, J. van den Brink, and J. P. Hill, Testing the Validity of the Strong Spin-Orbit-Coupling Limit for Octahedrally Coordinated Iridate Compounds in a Model System Sr_3CuIrO_6, Phys. Rev. Lett. **109**, 157401 (2012).

[31] M. Moretti Sala, K. Ohgushi, A. Al-Zein, Y. Hirata, G. Monaco, and M. Krisch, $CaIrO_3$: A Spin-Orbit Mott Insulator Beyond the $j_{\rm eff} = 1/2$ Ground State, Phys. Rev. Lett. **112**, 176402 (2014).

[32] M. K. Crawford, M. A. Subramanian, R. L. Harlow, J. A. Fernandez-Baca, Z. R. Wang, and D. C. Johnston, Structural and magnetic studies of Sr_2IrO_4, Phys. Rev. B **49**, 9198 (1994).

[33] M. Moretti Sala, C. Henriquet, L. Simonelli, R. Verbeni, and G. Monaco, High energy-resolution set-up for Ir L_3 edge RIXS experiments, J. Electron Spectrosc. Relat. Phenom. **188**, 150 (2013).

[34] M. Moretti Sala, K. Martel, C. Henriquet, A. Al Zein, L. Simonelli, Ch. J. Sahle, H. Gonzalez, M.-C. Lagier, C. Ponchut, S. Huotari, R. Verbeni, M. Krisch, and G. Monaco, A high-energy-resolution resonant inelastic X-ray scattering spectrometer at ID20 of the European Synchrotron Radiation Facility, J. Synchrotron Rad. **25**, 580 (2018).

[35] A. Revelli, M. Moretti Sala, G. Monaco, P. Becker, L. Bohatý, M. Hermanns, T. C. Koethe, T. Fröhlich, P. Warzanowski, T. Lorenz, S. V. Streltsov, P.H.M. van Loosdrecht, D. I. Khomskii, J. van den Brink, and M. Grüninger, Resonant inelastic x-ray incarnation of young's double-slit experiment, Sci. Adv. **5**, eaav4020 (2019).

[36] H. Wang and J. Zhou, Numerical conversion between the Pearson VII and pseudo-Voigt functions, J. Appl. Cryst. **38**, 830 (2005).

[37] J. Kim, D. Casa, M. H. Upton, T. Gog, Y.-J. Kim, J. F. Mitchell, M. van Veenendaal, M. Daghofer, J. van den Brink, G. Khaliullin, and B. J. Kim, Magnetic Excitation Spectra of Sr_2IrO_4 Probed by Resonant Inelastic X-Ray Scattering: Establishing Links to Cuprate Superconductors, Phys. Rev. Lett. **108**, 177003 (2012).

[38] A. M. Cook, S. Matern, C. Hickey, A. A. Aczel, and A. Paramekanti, Spin-orbit coupled $j_{\rm eff} = 1/2$ iridium moments on the geometrically frustrated fcc lattice, Phys. Rev. B **92**, 020417(R) (2015).

[39] A. A. Aczel, A. M. Cook, T. J. Williams, S. Calder, A. D. Christianson, G.-X. Cao, D. Mandrus, Y.-B. Kim, and A. Paramekanti, Highly anisotropic exchange interactions of $j_{\rm eff} = 1/2$ iridium moments on the fcc lattice in La_2BIrO_6(B = Mg, Zn), Phys. Rev. B **93**, 214426 (2016).

[40] F.-Y. Li, Y.-D. Li, Y. Yu, A. Paramekanti, and G. Chen, Kitaev materials beyond iridates: Order by quantum disorder and Weyl magnons in rare-earth double perovskites, Phys. Rev. B **95**, 085132 (2017).

[41] S. M. Winter, Y. Li, H. O. Jeschke, and R. Valentí, Challenges in design of Kitaev materials: Magnetic interactions from competing energy scales, Phys. Rev. B **93**, 214431 (2016).

[42] J. Reuther and P. Wölfle, J_1-J_2 frustrated two-dimensional Heisenberg model: Random phase approximation and functional renormalization group, Phys. Rev. B **81**, 144410 (2010).

[43] M. L. Baez and J. Reuther, Numerical treatment of spin systems with unrestricted spin length S: A functional renormalization group study, Phys. Rev. B **96**, 045144 (2017).

[44] F. L. Buessen, D. Roscher, S. Diehl, and S. Trebst, Functional renormalization group approach to SU(N) Heisenberg models: Real-space renormalization group at arbitrary N, Phys. Rev. B **97**, 064415 (2018).

[45] D. Roscher, F. L. Buessen, M. M. Scherer, S. Trebst, and S. Diehl, Functional renormalization group approach to SU(N) Heisenberg models: Momentum-space renormalization group for the large-N limit, Phys. Rev. B **97**, 064416 (2018).

[46] J. M. Luttinger and L. Tisza, Theory of dipole interaction in crystals, Phys. Rev. **70**, 954 (1946).

[47] J. M. Luttinger, A note on the ground state in antiferromagnetics, Phys. Rev. **81**, 1015 (1951).

[48] C. L. Henley, Ordering by disorder: Ground-state selection in fcc vector antiferromagnets, J. Appl. Phys. **61**, 3962 (1987).

[49] A similar scenario has recently been discussed in the context of the $J_1 - J_2$ Heisenberg model on the diamond lattice [55, 56].

[50] J. Reuther, R. Thomale, and S. Trebst, Finite-temperature phase diagram of the Heisenberg-Kitaev model, Phys. Rev. B **84**, 100406(R) (2011).

[51] H. Liu and G. Khaliullin, Pseudo-Jahn-Teller Effect and Magnetoelastic Coupling in Spin-Orbit Mott Insulators, Phys. Rev. Lett. **122**, 057203 (2019).

[52] A. A. Aczel, J. P. Clancy, Q. Chen, H. D. Zhou, D. Reig-i-Plessis, G. J. MacDougall, J. P. C. Ruff, M. H. Upton, Z. Islam, T. J. Williams, S. Calder, and J.-Q. Yan, Revisiting the Kitaev material candidacy of Ir^{4+} double perovskite iridates, Phys. Rev. B **99**, 134417 (2019).

[53] N. Khan, D. Prishchenko, Y. Skourski, V. G. Mazurenko, and A. A. Tsirlin, Cubic symmetry and magnetic frustration on the fcc spin lattice in K_2IrCl_6, Phys. Rev. B **99**, 144425 (2019).

[54] G. A. Bain and J. F. Berry, Diamagnetic corrections and Pascal's constants, J. Chem. Educ. **85**, 532 (2008).

[55] D. Bergman, J. Alicea, E. Gull, S. Trebst, and L. Balents, Order-by-disorder and spiral spin-liquid in frustrated diamond-lattice antiferromagnets, Nat. Phys. **3**, 487 (2007).

[56] F. L. Buessen, M. Hering, J. Reuther, and S. Trebst, Quantum Spin Liquids in Frustrated Spin-1 Diamond Antiferromagnets, Phys. Rev. Lett. **120**, 057201 (2018).

[57] D. Elwell and H. J. Scheel, *Crystal Growth from High-Temperature Solutions* (Academic Press, London, New York, San Francisco, 1975).

[58] B. Yuan, J. P. Clancy, A. M. Cook, C. M. Thompson, J. Greedan, G. Cao, B. C. Jeon, T. W. Noh, M. H. Upton, D. Casa, T. Gog, A. Paramekanti, and Y.-J. Kim, Determination of Hund's coupling in 5d oxides using resonant inelastic x-ray scattering, Phys. Rev. B **95**, 235114 (2017).

[59] A. Nag, S. Bhowal, A. Chakraborty, M. Moretti Sala, A. Efimenko, F. Bert, P. K. Biswas, A. D. Hillier, M. Itoh, S. D. Kaushik, V. Siruguri, C. Meneghini, I. Dasgupta, and S. Ray, Origin of magnetic moments and presence of spin-orbit singlets in Ba_2YIrO_6, Phys. Rev. B **98**, 014431 (2018).

[60] P. E. Blöchl, Projector augmented-wave method, Phys. Rev. B **50**, 17953 (1994).

[61] G. Kresse and J. Furthmüller, Efficient iterative schemes for *ab initio* total-energy calculations using a plane-wave basis set, Phys. Rev. B **54**, 11169 (1996).

[62] J. P. Perdew, K. Burke, and M. Ernzerhof, Generalized Gradient Approximation Made Simple, Phys. Rev. Lett. **77**, 3865 (1996).

[63] S. L. Dudarev, G. A. Botton, S. Y. Savrasov, C. J. Humphreys, and A. P. Sutton, Electron-energy-loss spectra and the structural stability of nickel oxide: An LSDA+U study, Phys. Rev. B **57**, 1505 (1998).